

An Automatic Detection System of Lung Nodule Based on Multigroup Patch-Based Deep Learning Network

Hongyang Jiang, He Ma^{ID}, Wei Qian^{ID}, Mengdi Gao, and Yan Li

Abstract—High-efficiency lung nodule detection dramatically contributes to the risk assessment of lung cancer. It is a significant and challenging task to quickly locate the exact positions of lung nodules. Extensive work has been done by researchers around this domain for approximately two decades. However, previous computer-aided detection (CADe) schemes are mostly intricate and time-consuming since they may require more image processing modules, such as the computed tomography image transformation, the lung nodule segmentation, and the feature extraction, to construct a whole CADe system. It is difficult for these schemes to process and analyze enormous data when the medical images continue to increase. Besides, some state of the art deep learning schemes may be strict in the standard of database. This study proposes an effective lung nodule detection scheme based on multigroup patches cut out from the lung images, which are enhanced by the Frangi filter. Through combining two groups of images, a four-channel convolution neural networks model is designed to learn the knowledge of radiologists for detecting nodules of four levels. This CADe scheme can acquire the sensitivity of 80.06% with 4.7 false positives per scan and the sensitivity of 94% with 15.1 false positives per scan. The results demonstrate that the multigroup patch-based learning system is efficient to improve the performance of lung nodule detection and greatly reduce the false positives under a huge amount of image data.

Index Terms—Computer aided detection (CADe), computed tomography (CT) images, deep learning network, Frangi filter, lung nodule detection.

Manuscript received December 29, 2016; revised May 2, 2017 and June 11, 2017; accepted July 6, 2017. Date of publication July 13, 2017; date of current version June 29, 2018. This work was supported in part by the Recruitment Program of Global Experts under Grant 01270021814101/022, in part by the Fundamental Research Funds for the Central Universities under Grant N151903002/N150408001, and in part by the Bureau of Science and Technology of Liaoning Province under Grant 201501146. (*Corresponding author: He Ma*.)

H. Jiang and M. Gao are with the Sino-Dutch Biomedical and Information Engineering School, Northeastern University, Shenyang 110819, China (e-mail: hongyang1020@126.com; neugaomengdi@126.com).

H. Ma is with the Sino-Dutch Biomedical and Information Engineering School and the Key Laboratory of Medical Image Computing, Ministry of Education, Northeastern University, Shenyang 110819, China (e-mail: maha@bmie.neu.edu.cn).

W. Qian is with the Sino-Dutch Biomedical and Information Engineering School, Northeastern University, Shenyang 110819, China, and also with the College of Engineering, University of Texas at El Paso, El Paso, TX 79968 USA (e-mail: wqian@utep.edu).

Y. Li is with the Troops 31411 of People's Liberation Army, Shenyang 119402, China (e-mail: xiaohair_99@163.com).

Digital Object Identifier 10.1109/JBHI.2017.2725903

I. INTRODUCTION

LUNG cancer is one of the most widespread diseases and leads to the highest mortality among all the forms of cancer. As is reported in global cancer statistics in 2012, nearly 1.83 million new cases of lung cancer occurred and the estimated deaths are over 1.5 million [1]. The causes of lung cancer include smokes, toxic particles in the air, aging, gene, gender, etc. Unfortunately, people feel incapable of finding useful ways to curb the incidence of cancer and meanwhile it is almost impossible to find a cure when patients are in the terminal stage of cancer under the current condition. The confirmed cases of lung cancer are commonly accompanied by continuing emergence of nodules. Early detection of cancer can greatly improve survival rates of patients. Distinctly, the lung nodule detection in the initial stage of computer-aided diagnosis (CADx) schemes is remarkable and obligatory.

After decades of years' development and verification, the computed tomography (CT) imaging technique can generate high resolution, low distortions and strong contrast of anatomical structures in the chest which is sensitive to the lung cancer detection [2]. Thus, more and more medical CT images were accumulated in hospital and need to be further diagnosed by the radiologist. However, screening these enormous pathological images consumes plenty of time and effort. Meanwhile, it is also error-prone for the radiologist to detect lots of nodules because of fatigue. To alleviate this problem, CAD schemes are urgently required to share responsibility for the detection work. The main functions of CAD systems are lesion detection, lesion body segmentation and pathological analysis by means of image processing techniques and machine learning algorithms [3]. These CADs immensely improve the efficiency of detection and diagnosis and can rectify some possible errors. Academically, lung nodules are divided into the benign and the malignant and all of them roughly consist of solitary, juxta-vascular, juxta-pleural, ground glass and small nodules [4]. However, lung nodules own various shapes, scales and densities, which can hardly be generalized to specific categories. The difference of nodules increases the difficulty of lung nodules detection, so it is very meaningful for investigators to put forward some potential CADe schemes to achieve more well-pleasing detection performance.

The lung nodule detection is an important research domain thus scholars have been focusing on this field for about twenty years. With the upgrades of the imaging equipment, lung CT images of high quality lay a solid foundation for the nodule

detection. Multifarious nodule detection methods based on CADe schemes developed quickly and obtained preferable results over the past five years [5]–[14].

Maxine Tan *et al.* picked out nodule candidates based on filters of nodule and vessel enhancement and located the centers of the nodule clusters in detection stage. After that, invariant features were extracted for differentiating real and false nodules based on genetic algorithms and artificial neural networks (ANNs) in classification stage [5]. Wook-Jin Choi *et al.* proposed three-dimensional shape-based feature descriptor to detect lung nodules. Nodule candidates were detected through multi-scale dot enhancement filtering and feature descriptors were extracted from these nodules, which were used for classification by means of support vector machine (SVM) [6]. Diego M. Peña *et al.* selected possible nodule candidates through 3D blob algorithm related to connectivity algorithms. On this basis, eight minimal representative features were extracted for distinguishing between true nodules and false positives using SVM classifier [7]. Erda I Taşciet *et al.* designed a novel system which can provide automatic detection of juxta-pleural nodule. Shape and texture based features were considered for nodule detection and final 33 features were contributed to that literature [8]. Alex Martins Santos *et al.* had the purpose of inventing a method for automatic detection of small nodules (diameters between 2 and 10 mm). lung parenchyma was segmented through region growing technique and structures inside lung were segmented by Gaussian mixture models and Hessian matrix. Tsallis's and Shannon's entropy measurements as texture features helped to classify suspect nodule regions based on SVM [9]. D. Cascio *et al.* developed a CAD system for internal and juxta-pleural nodules detection. To solve the problem of suspected nodular lesions segmentation and extraction, they utilized a stable 3D Mass-Spring Model (MSM) associated with a spline curves reconstruction. Furthermore, the neural network was applied to reduce false positives based on the gray value, contour and shape features extracted from nodule candidates [10]. S.Sivakumar *et al.* adopted fuzzy based clustering models to perform nodule segmentation in their CAD schemes. Moreover, they used SVM with three different kernel functions to acquire good classification results [11]. N.Camarlinghi *et al.* combined three different computer-aided detection (CADe) systems developed by investigators of the Italian MAGIC-5 collaboration to increase the accuracy of lung nodules identification [12]. Hoo-Chang Shin *et al.* attempted to evaluate the performance of different deep convolution neural networks (CNN) and studied transfer learning to solve two CADe problems: thoraco-abdominal lymph node detection and interstitial lung disease classification [13]. Rushil Anirudh *et al.* tried to apply 3D CNN to discriminative features learning for lung nodule detection. To solve the problem of lack of labels, they used unsupervised partition method to grow out 3D regions based on the central pixels of nodules [14].

In view of the characteristics of these methods, CADe systems can be divided into two types: the manual feature selection system [15]–[18] and the automatic feature learning-oriented system [19]–[22]. The first type usually required complicated nodule segmentation steps and incomplete feature selection strategies for better analysis. As medical images were increasingly accumulated, superfluous processing procedures cost

more time and space complexity. However, the training data of the second type were rough and lacked pertinence. Inspired by the strong analytic ability of deep learning that has been applied to medical images [23], [24], this study proposed a novel CADe scheme to automatically detect lung nodules based on the CNN structure. Besides, this study tried to use multi-group 2D lung CT images for nodules detection. First, the distorted lung contours caused by juxta-pleural nodule were repaired through a slope analysis method designed by this study. Second, vessel-like structures in lung CT images were eliminated through Frangi filters of adjustable parameters. Finally, a novel deep learning network, that is a CNN structure, was designed to learn the knowledge of radiologists using two groups of images. Group 1 consists of original lung CT images and Group 2 consists of binary images that are generated through complex binarization processing on Group 1, which is illustrated in next sections. This study therefore can sample many pairs of sub-images from any one of the original images (Group 1) and its binary image (Group 2) in the same position. The pairs of sub-images were just the input images of the CNN model. This CADe scheme for lung nodule detection can acquire quite outstanding results and save much storage space and processing time.

II. MATERIAL AND METHODS

A. Data Set Preparation

The database used in this work is LIDC/IDRI that is a public database. The database contains a total of 1018 helical thoracic CT scans acquired from 1010 different patients. The process of annotating the nodules of the LIDC/IDRI database was performed by four radiologists in two stages. In the first stage, each radiologist analyzed the exams individually. In the second stage, the results of the four analyses of the first stage were presented together to the four radiologists. During this stage, each of the radiologists re-analyzed the exams and again made their annotations independently [25]. Accordingly, each case in LIDC/IDRI database has a XML file to record these radiologists' annotations. These lung CT images were saved as the DICOM format that is one of the popular standard in medicine and some imaging parameters of each lung CT image, including slice thickness and pixel spacing, can be checked from them [26]. As lung CT images in the LIDC/IDRI database were collected by different imaging devices, we normalized the pixel spacing of each image for recognizing the actual sizes of 2D nodules. The standardized pixel spacing was set to 0.688 mm that is the mean value of all the pixel spacing. The nodules annotated by radiologists have been classified into two kinds of nodules: small nodules whose diameters were less than 3 mm and big nodules whose diameters were more than 3mm. In addition, the radiologists have marked the central points of the small nodules and the contours of the big nodules. As small nodules (<3 mm) are labelled by only central points and easily corroded by image filters, it is inappropriate for this proposed method to detect small nodules. Therefore, the main task of this study is to automatically detect big nodules (>3 mm), which can be demonstrated in later sections.

1006 scans that have annotation XML files were used in this study. As the information in these XML files were not convenient to read directly, we designed a kind of data storage structure to

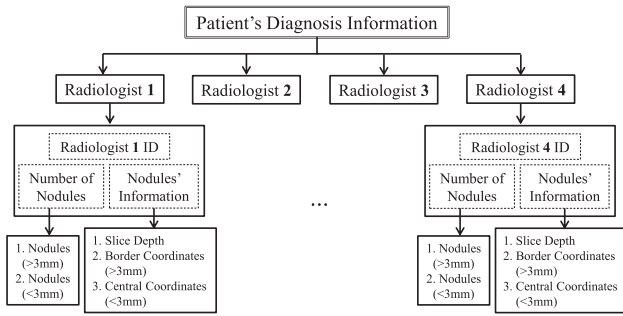


Fig. 1. The data storage structure of patient.

store four radiologists' annotations. Each radiologist had an identification (ID) and annotation messages including the number of nodules and nodules' pathological attributes. The details of this structure are displayed in Fig. 1. Hence, we transformed the XML files into a group of patients' data structures which can be automatically and programmatically extracted for our experiments. In addition, this study took the agreement level 1, whose definition is that a nodule that is annotated by at least 1 radiologist, can be considered as a true nodule, as a golden standard to mark the true nodules for validating our method [27].

The sizes of nodules may be either too big or too small and had different effect on detection. In this study, a total of 25723 two-dimensional nodules (>3 mm) in these CT slices were contained in 1006 cases.

B. Lung Contour Mending and Parenchyma Segmentation

The content of a provided lung CT image in LIDC/IDRI contained imaging region and non-imaging region which are shown in Fig. 2(a). Apparently, a circular region is the imaging region and contains machine tool, clothes, thorax, skeleton, lung lobes, fatty tissue etc, whereas the region outside the circle is the non-imaging region. To perfectly extract the lung parenchyma, an automatic segmentation scheme proposed by this study was accomplished by four steps. The processing procedure of lung parenchyma segmentation can be seen in Fig. 3.

First step, the brightness of lung and extrathoracic region is appreciably darker than chest area in the CT images, thus the shape of lung was highlighted through local maximum variance between clusters [28]. Second step, according to common sense about the lung shape and position, this study adopted the connected region (4 or 8 neighborhood) analysis and the morphological method including opening and closing operations to eliminate noises outside the lung region, such as the esophagus. At the same time, a padding operator, whose area was much less than lung lobes, was used to fill the bubbles inside the lung and enhance the contour of lung [29]. Third step, this study designed

a fast method of mending the lung contour for juxta-pleural nodules which are lung tumors near the thorax wall. Juxta-pleural nodules were easily left out and were probability considered as regions outside the lung compared with other types of nodule. Considering this problem, this study used two sizes of patches, a 32 pixels \times 32 pixels block and a 16 pixels \times 16 pixels block, to scan the lung contour. In addition, the scanning direction of the patch can be right, left, down or up, which is shown in Fig. 2(b). The patch can automatically adjust its scanning direction in accordance with the angle of lung contour and Fig. 2(c) shows the process of contour scanning. This study mainly focused on mending the relatively smooth contour of lung and most juxta-pleural nodules appeared against the smooth lung contour by observing vast cases. Within each patch, the changes of lung contour slope were analyzed by the difference method and we can judge that whether the positions need to be repaired. Once one juxta-pleural nodule was detected to be neglected, the boundary can be repaired automatically based on its position in the lung. Last step, the lung parenchyma was segmented by the corrective lung contour. Fig. 2(d) shows the segmentation results of the lung and the dotted red circles mark the positions of the repaired nodules.

C. Vessel Elimination

A volume of detailed tissues was contained in lung parenchyma including nodules, vessels, or other impurities. Notably vascular morphology was so conspicuous inside the lung that they may affect the detection performance of lung nodules. In lung CT images, all the pixels of vessels and nodules emerged as bright tissues among the darker adjacent pixels. However, the morphology and structure of vessels were obviously distinct from those of lung nodules. In general, vessels looked like tubular structures, whereas lung nodules appeared as ellipse, irregular sphere or cotton-like structures. The aim of this step was to eliminate the vascular structures in the lung, thus we can beneficially analyze nodule-like structures. Some mature vessel enhancement algorithms such as Sato filter, vessel enhancing diffusion (VED) filter and Frangi filter has been proposed by previous researchers [30]–[32]. These vascular enhancement filters were mainly applied to retina and achieved good results [33]–[35]. Among these algorithms, the Frangi filter was widely recognized as the gold-standard for vascular enhancement which can effectively enhance vessel-like structures and meanwhile largely weaken other structures [36]. Hence, in view of the characteristic of vessels inside the lung this study designed a method to eliminate vascular structures based on multi-scale Frangi filter.

As was described in [32], one image $I(x, y)$ can be expressed as a Taylor expansion in the neighborhood of a random point $p(x_0, y_0)$. The second-order term of the Taylor expansion contained the Hessian matrix of $I(x, y)$, which is denoted as $H_{p,\sigma}$.

$$H_{p,\sigma} = \begin{bmatrix} I(x, y) \otimes \left(\frac{\partial}{\partial x} \right) \left(\frac{\partial}{\partial x} \right) G(x, y) & I(x, y) \otimes \left(\frac{\partial}{\partial x} \right) \left(\frac{\partial}{\partial y} \right) G(x, y) \\ I(x, y) \otimes \left(\frac{\partial}{\partial x} \right) \left(\frac{\partial}{\partial y} \right) G(x, y) & I(x, y) \otimes \left(\frac{\partial}{\partial y} \right) \left(\frac{\partial}{\partial y} \right) G(x, y) \end{bmatrix} \quad (1)$$

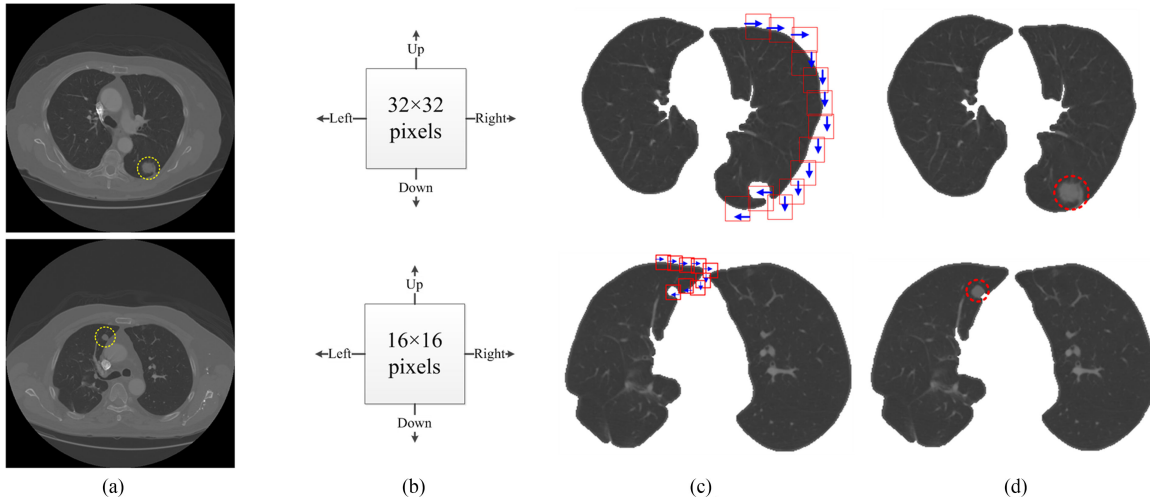


Fig. 2. Performance of lung contour mending and parenchyma segmentation. **(a)** Raw lung CT images: yellow dotted circles mark the position of juxta-pleural nodules; **(b)** Two sizes of mending patches: 16×16 pixels and 32×32 pixels; **(c)** The process of scanning the lung contours; **(d)** The repaired lung contours: red dotted circles mark the repaired juxta-pleural nodules.

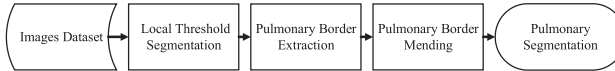


Fig. 3. Flow chart for lung parenchyma segmentation.

Here p represents $p(x_0, y_0)$ and σ is denoted as the scale of Gaussian kernel $G(x, y)$ which is expressed as (2). Thus $H_{p,\sigma}$ can be calculated by (1) shown at the bottom of the previous page and (2). $H_{p,\sigma}$ is a matrix that consists of the convolutions of the image $I(x, y)$ and the second-order differential of $G(x, y)$ with respect to x or y .

$$G(x, y) = (1/2\pi\sigma^2) \cdot \exp(-\|(x, y)\|^2/2\sigma^2) \quad (2)$$

We therefore get the Hessian matrix ($H_{p,\sigma}$) which will be further analyzed for the vascular detection. The eigenvalues and eigenvectors of $H_{p,\sigma}$, which are denoted as λ_k and μ_k ($k = 1, 2$) respectively, are both calculated under the scale of σ . For a two-dimensional (2D) image, two eigenvalues (λ_1 and λ_2) represent different detection structures. μ_1 indicates the direction along the vessel and μ_2 is the orthogonal direction of μ_1 . λ_1 and λ_2 play a decisive role in discriminating local vascular orientation. To detect bright vessel-like structure, λ_1 and λ_2 should satisfy two conditions: (a) $|\lambda_1| \approx 0$; (b) $|\lambda_1| \ll |\lambda_2|$. The measure formula of vessel likeliness is displayed in (3) shown at the bottom of this page, by using the two eigenvalues (λ_1 and λ_2).

The parameters β_1 and β_2 are adjustable thresholds which can control the filters' sensitivity to $|\lambda_1/\lambda_2|$ and 2-norm $\|(\lambda_1, \lambda_2)\|$. $|\lambda_1/\lambda_2|$ is essential for differentiating the vessel-like and nodule-like structures and $\|(\lambda_1, \lambda_2)\|$ can reflect the contrast of the object and the background. According to the gray scale of images

used in this study, β_1 and β_2 were set to 0.6 and 20 respectively. The aim of this study was to eliminate the vessel structures in lung CT images but not to enhance the vessels. So, the method of vessels elimination was designed in two steps. First, the vessel structure image was created through the Frangi filter under the optimal scale of σ . Second, the generated vessel structure image was subtracted from the original lung image and then we obtained the vessel eliminated images. The vessel elimination performance of three cases are displayed in Fig. 4. In these cases, the raw images with vascular structures and the vessel-eliminated images under three different scales are shown for comparison. Column (b) shows the effect of $\sigma = 1$ and some vascular structures were still clear although the nodules are distinct. However, the nodules were deformed slightly by changing the value of σ to 2, which are shown in column (d). Through observation, the vessel-like structures were largely eliminated and the distortion of nodule-like structures were unobvious when the value of scale σ was set to 1.5.

After vascular elimination, the image threshold processing method (OTSU) was taken on the vessel-eliminated images. Through comparison in Fig. 5, we can see that binary images Fig. 5(c) contained less suspicious nodules than Fig. 5(b), thus using this vessel elimination method had two advantages:

- 1) The method can decrease the number of suspicious regions that need to be judged later and meanwhile improve the nodule detection rate.
- 2) The number of false positives can be reduced.

D. Convolution Neural Network for Nodule Detection

Normalizing the data set: Generally, the original image contained many meaningless objects and only a small number of regions need further analysis. This study designed a data

$$V_p = \begin{cases} 0 & \text{if } \lambda_2 > 0 \\ \exp\left(-|\lambda_1/\lambda_2|^2/2\beta_1^2\right) \left(1 - \exp\left(\left(\|\lambda_1, \lambda_2\|\right)^2/2\beta_2^2\right)\right) & \text{otherwise} \end{cases} \quad (3)$$

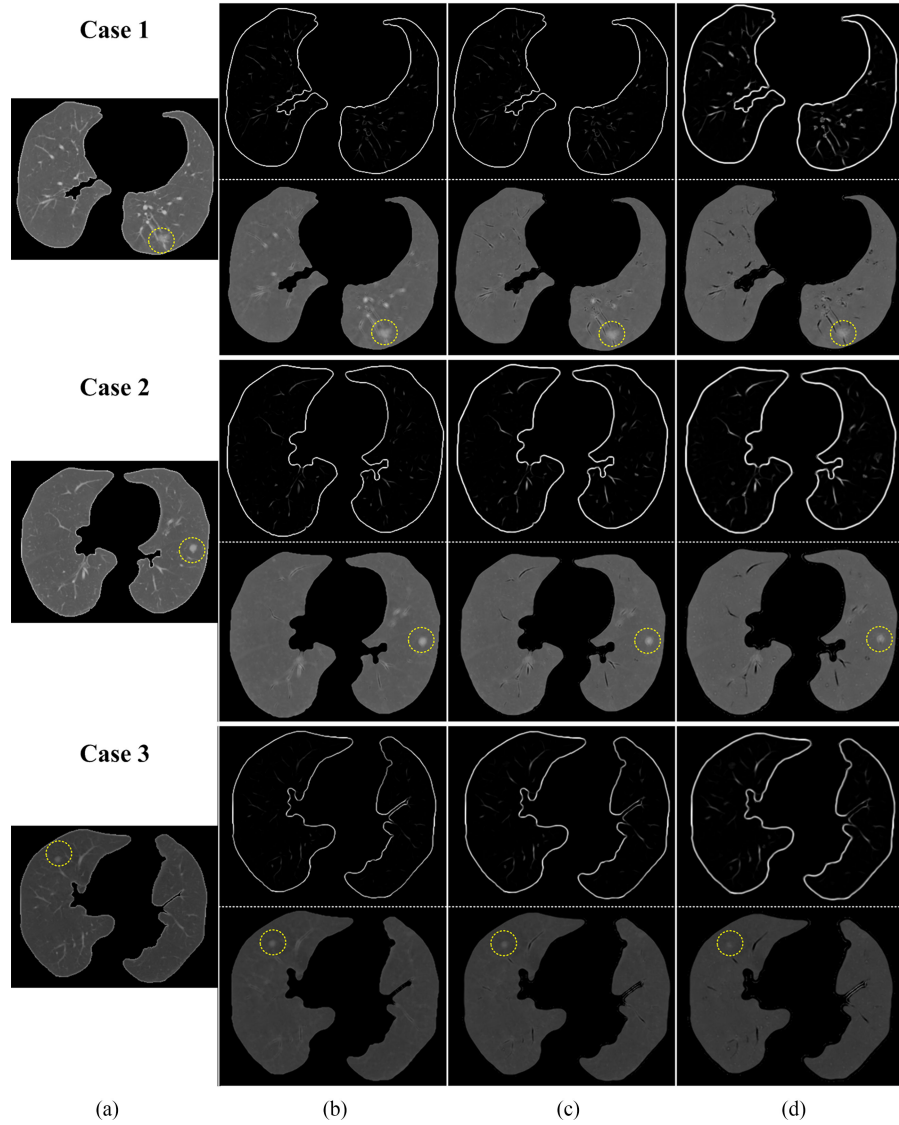


Fig. 4. Performance comparison of vessel elimination under three different scales of Gaussian kernel $G(x, y)$: Column (a) are the original lung images; Column (b), (c) and (d) are the results of vessel elimination under $\sigma = 1, 1.5$ and 2 respectively. The regions of the nodule are marked by yellow dotted circles.

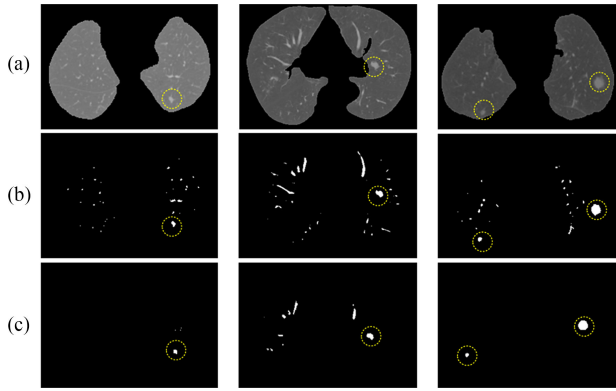


Fig. 5. Image binarization comparison between the original lung image and the vessel-eliminated images. (a) Original lung; (b) Binary image of original lung; (c) Binary image generated after vascular elimination of original lung.

normalization method to collect a more significant data set (see Fig. 6). Obviously, nodules in the images without vascular structures can be easily recognized by radiologists and even by laymen. Moreover, we can just reserve the regions of suspected nodule lesions and exclude the others by sampling both the original image and the binary image of vessel-eliminated lung image. After collecting all these suspected samples, this study adjusted the object in the center of the sample image, that is, object centralization. In Fig. 6, parameters h_1 , h_2 , w_1 and w_2 should satisfy $h_1 = h_2$ and $w_1 = w_2$. Then the normalized data set was formed (Data Set 2).

CNN architecture design: CNN is one of the most popular deep learning techniques that can automatically extract image features. In general, a CNN architecture includes convolutional (CONV) layer, pooling layer and fully connected (FC) layer. Besides, this study utilized rectified linear unit (ReLU) function to replace the traditional activation functions after the

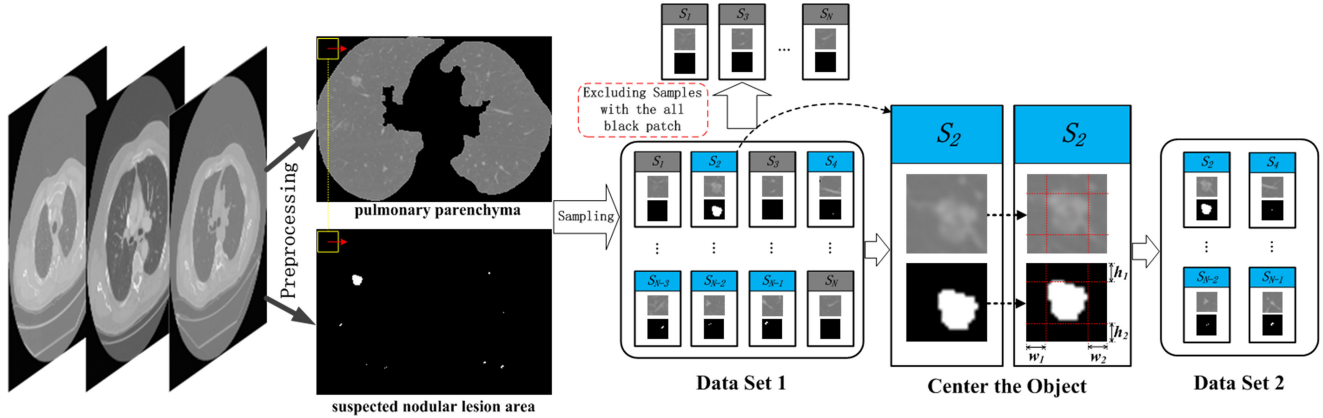


Fig. 6. Normalization process of suspected nodular lesions. First, segmenting the lung parenchyma from the raw lung CT image and then generating the binary image of vessel-eliminated lung image. Second, simultaneously sampling both the two images on the same position and generating **Data Set 1**. Third, excluding samples that contains the all black patch. In the end, centering the objects of the samples and generating **Data Set 2**.

convolution layers. The outstanding advantage of ReLU is that it can help the CNN structure faster reduce the training error rate than other activation functions [37]. ReLU function behind the CONV layer is expressed as

$$y_i = \max \left(0, \sum_j k_{ji} * x_j + b_i \right) \quad (4)$$

where symbol “*” denotes the convolution operation, and x_j and y_i represents the input map and output map respectively. Besides, k_{ji} is the convolutional kernel between the j th input map and i th output map. Besides, b_i is indicated as the bias of the i th output map. Both parameters k_{ji} and b_i can be learned during the training process. As for the pooling layer, universal operations are max-pooling and average-pooling. This study took a kind of multi-crop (MC) pooling operation as the pooling layer [37], [38]. The MC pooling operation can be depicted as

$$y_i = MC_i(x), i = \{0, 1\} \quad (5)$$

$$MC_i(x) = \begin{cases} MP(x) & i = 0 \\ CP_i(x) & i = 1, 2, \dots \end{cases} \quad (6)$$

where x is the input map and y_i is the output map. We assumed that the size of x is $L \times L$. MP denotes the max-pooling operation and the size of $MP(x)$ is $(L/2) \times (L/2)$. CP represents the center-pooling operation, which means that $CP_1(x)$ is the center region cropped from x and the size of $CP_1(x)$ is $(L/2) \times (L/2)$. In the same way, $CP_i(x)$ is the center region cropped from $CP_{(i-1)}(x)$, thus the size of $CP_2(x)$ is $(L/4) \times (L/4)$. We defined the MC_i as the i th order MC processing. The process of MC pooling operation can be illustrated in Fig. 7. To predict whether a suspected region was a nodule or not, we adopted 2-way softmax. Moreover, using the stochastic gradient descent backpropagation this study minimized the softmax log-loss function which is expressed as

$$J = - \sum_{k=1}^C \log \left(\frac{e^{x_k}}{\sum_i^C e^{x_i}} \right) \quad (7)$$

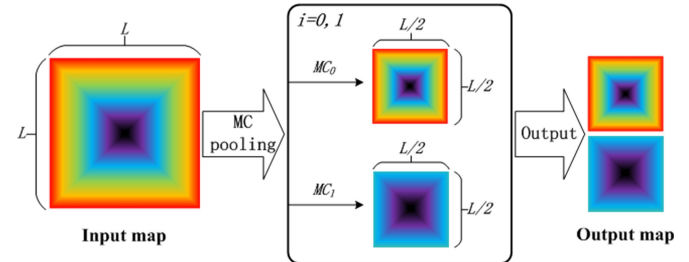


Fig. 7. The process of MC pooling operation. This study adopted first order MC processing. MC_0 is max-pooling operation and MC_1 is center-pooling operation.

TABLE I
DESCRIPTIONS OF FOUR DETECTION LEVELS

Level	DN(mm)	ASS(mm^2)	PSS($N \times N$)
1	3–7	189.33	20×20
2	8–12	272.65	24×24
3	13–17	371.10	28×28
4	above 17	484.70	32×32

DN = Diameter of Nodule, ASS = Actual Size of Sub-Images, PSS = Pixel Size of Sub-Images

where x_i is the output of the network and C is the number of classes which was set to 2 here. The detail CNN structures are shown in Fig. 8. This study created different sizes of sampling patches including 32×32 , 28×28 , 24×24 and 20×20 pixels for detecting different sizes of object (see Table I). The four different patches can divide the sizes of nodules into four different ranges of sizes, which can improve the detection accuracy through experiments. Besides, the four patches with preset dimensions will become the input images of CNN, which can benefit the construction of CNN structure. Each input of the CNN channel is a pair images that cropped from the same position of the original image. Considering the original sizes of input images, this study applied a two-order MC pooling operation that followed each ReLU operation. Accordingly, more details

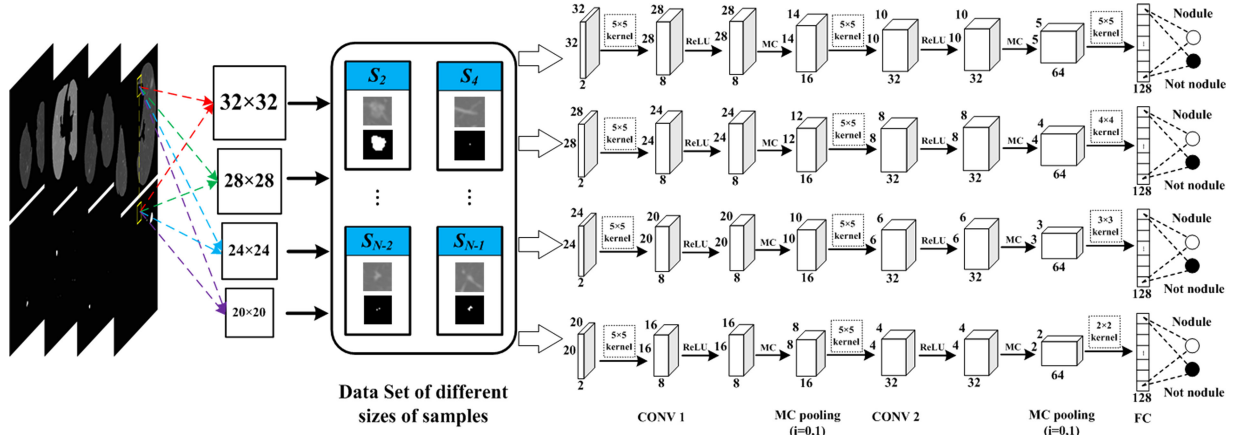


Fig. 8. The process of MC pooling operation. This study adopted first order MC processing. MC_0 is max-pooling operation and MC_1 is center-pooling operation.

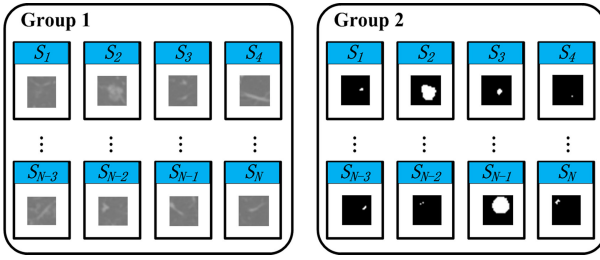


Fig. 9. Two groups of image data. Group 1 and 2 represented the original sub-images and thresholding processed sub-images, respectively.

of objects in the images can be provided, which was proved to be an efficient method for improving the performance of nodule detection [38]. For each channel, we utilized a convolution layer before the FC layer to generate 128 nodes which were the input of FC layer.

E. Nodule Level Classification and Segmentation

First, we defined two groups of image data. Group 1 contained images that are cropped from the original lung images; Group 2 contained binary images that are cropped from the vessel-eliminated lung images (see Fig. 9). As mentioned above, this study used both the two groups of data. Second, we divided the nodules into four levels from the small to the large based on the sizes of them (see Table I). As the diameters of nodules approximately ranged from 3 mm to 30 mm which were reckoned by four radiologists, the size variation may influence the detection precision. In this situation, detecting each level of nodules separately may help improve the performance. In this study, each level of nodules required its special detection patch window, which is a sub-image from the original lung image. The size of sub-image (actual size and pixel size) was specified thus we can cut the corresponding sub-images and build them into Group 1 and 2. The detailed descriptions of nodule levels are displayed in Table I. In addition, different levels of nodules are displayed in Fig. 10.

In Fig. 10, images appeared in pairs including A_i ($A_i - 1, A_i - 2$), B_i ($B_i - 1, B_i - 2$), C_i ($C_i - 1, C_i - 2$) and D_i ($D_i - 1, D_i - 2$) ($i = 1, 2, 3$). Nodules in A_i, B_i, C_i and D_i belonged

to grade level 1, 2, 3 and 4 respectively. The first row ($A_i - 1, B_i - 1, C_i - 1$ and $D_i - 1$) was the processed lung image that contained the nodule positions labeled by radiologists. The second row ($A_i - 2, B_i - 2, C_i - 2$ and $D_i - 2$) was the results of threshold segmentation of the first row. Because the difference of pixel value between the background and the object was small, OTSU threshold had little effect on segmenting the object, especially the nodule. Thus, this study used (8) to search a preferable threshold value.

$$T = (1 - \lambda) \cdot \left[\left(\sum_{i=1}^N p_i \right) / N \right] + \lambda \cdot \max(p_i), 1/2 \leq \lambda \geq 2/3 \quad (8)$$

In (8), p_i represents the pixel value in the lung parenchyma, N is the total number of pixels of lung parenchyma and λ is an adjustable parameter. The segmentation effectiveness was favorable when λ was set to between 1/2 and 2/3. Through analyzing the pixel values between the nodule region and the background region, this study set the value of λ to 5/9. Therefore, we eliminated the background and segmented the objects including nodules and few residues of vessels. Under this condition, all meaningless sub-images, such as all black images, were not taken as the input images of CNN structure.

III. EXPERIMENT AND RESULTS

Through merging Group 1 and 2 that is denoted as Group 1&2, we can improve the detection performance obviously. To demonstrate the superiority of Group 1&2, this study tested the effectiveness of both the Group 1&2 and Group 1. During this experiment, the amount of non-nodule images used for training and testing were the same to that of nodule images. After the 10-fold cross validation, Fig. 11(a)-(d) display the receiver operating characteristic (ROC) curves of them between true positive rate (sensitivity) and false positive rate (1-specificity).

Through comparison, the detection performance of Group 1&2 prevailed over that of Group 1. Besides, the area under the curve (AUC) of Group 1 can get better as the size of nodule candidates become bigger. Table II shows the detailed comparison of performance indicators, including sensitivity, specificity, AUC and data size. All the indicators of using Group 1&2 are

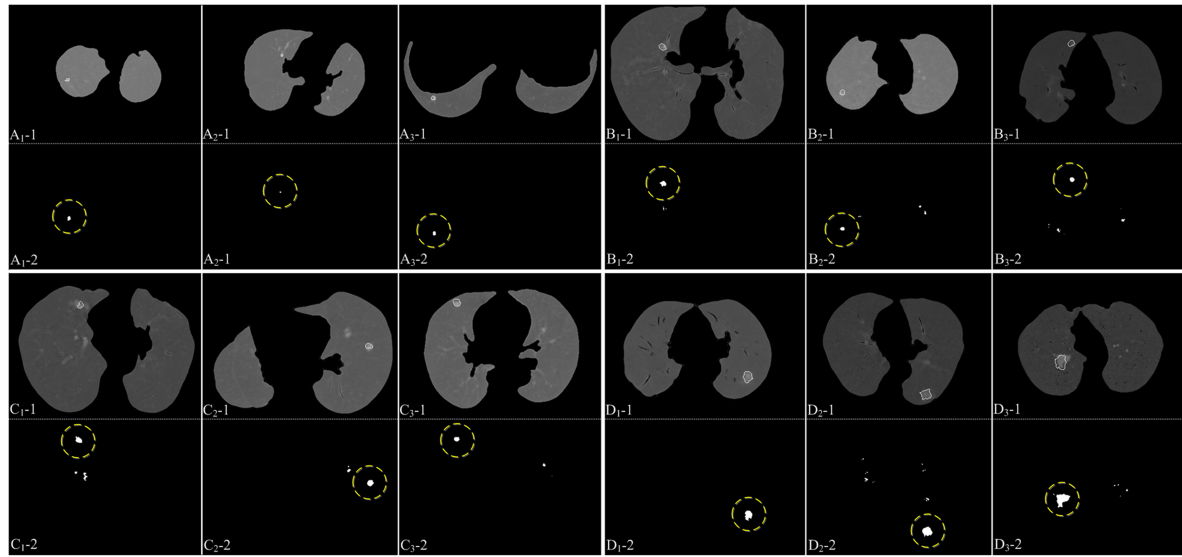


Fig. 10. Processed images that contained different grade levels of the nodule. Nodules in A, B, C and D represents level 1, 2, 3 and 4 respectively.

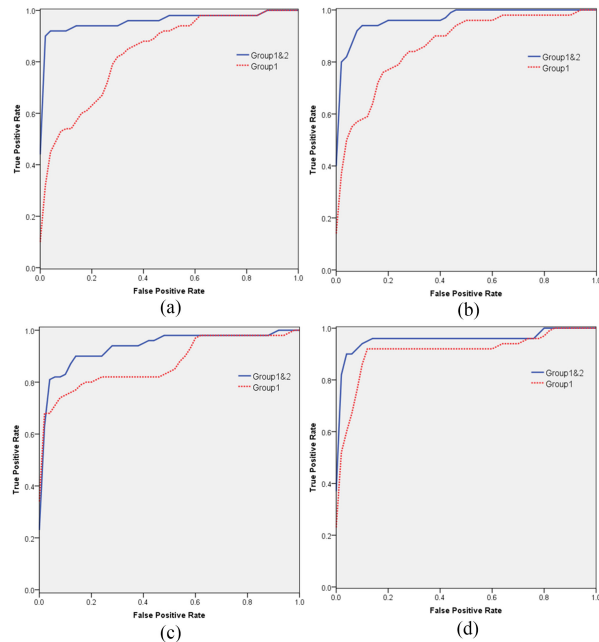


Fig. 11. ROC curves of four different grade levels of nodules. Solid blue lines represent ROC curves of Group 1&2 and dotted red lines represent the ROC curves of Group 1. (a) ROC curves under level 1 (b) ROC curves under level 2 (c) ROC curves under level 3 (d) ROC curves under level 4.

better than those of using Group 1. It is known that the activation function of CNN architecture can also conduct threshold operation, but this will increase the size of input data and the CNN architecture need another ‘drop-out’ regularization method for reducing over-training. Hence, it is unskillful to put all the raw data into the CNN. On the contrary, using threshold processing on Group 1 can not only reduce the size of input data of CNN, but also save much training time.

Through investigation, other researchers did not classify the nodules based on the sizes of them when they implemented the nodule detection strategy. This study demonstrated that it

can be meaningful to detect different sizes of nodules (level 1, 2, 3, 4) separately. Based on the existing annotation of radiologists, this study made a statistical analysis of the nodules sub-images distribution of four different levels in 2D lung slices (see Fig. 12). Besides, a total of about 275 thousand non-nodule sub-images were contained in Group 1&2. We can see that small size of nodules have further quantity than large size of nodules. Although nodules can be classified to four different types based on their status in the lung, this can hardly help us for the nodule detection but contribute to the nodule classification, which is not the focus of this study. In this experiment, we tried to take two ways of nodule detection and compared their performance. One way was detecting nodules without classification (single level detection) like other researchers. The other way was merging the performance of four independent detections (multi-level detection) under four different nodule levels proposed by this study. This study utilized the free response receiver operation characteristic (FROC) to characterize the detection performance of the two ways. When detected nodules matched radiologists’ annotations, then these nodules were checked out correctly. Using 10-fold cross-validation, we merged the detection results of four levels. Fig. 13 shows the FROC curves of nodule detection under level 1, 2, 3, 4, respectively. The performance of them were much the same overall. However, the higher of the level, the smaller of the false positives per scan at the initial points of the FROC curves, which demonstrates that the distributions of false positives under four nodule levels are still different. Hence, it is significant for us to divide four different nodule levels for helping the nodule detection. In addition, final FROC curves of the classified nodule detection and unclassified nodule detection can be illustrated in Fig. 14, which means that classified nodule detection can reduce the false positives around the whole data set.

In the experiment, all the programs of the experiments were executed on the server which had a 64-bit operating system, 128 GB RAM and quad-core processor of Intel Xeon CPU E7-4809 with the main frequency of 1.9 GHz. Besides, the CNN program frame used in this study was Matconvnet that was

TABLE II
STATISTICAL ANALYSIS RESULTS OF GROUP 1&2 AND GROUP 1 UNDER DIFFERENT NODULE LEVELS

Data set	level 1		level 2		level 3		level 4	
	Group 1&2	Group 1						
Sensitivity	0.935 ± 0.008	0.776 ± 0.011	0.955 ± 0.003	0.804 ± 0.006	0.913 ± 0.003	0.740 ± 0.004	0.937 ± 0.004	0.913 ± 0.003
Specificity	0.918 ± 0.005	0.865 ± 0.008	0.904 ± 0.013	0.818 ± 0.003	0.902 ± 0.002	0.941 ± 0.002	0.972 ± 0.002	0.901 ± 0.001
AUC	0.951 ± 0.006	0.855 ± 0.003	0.970 ± 0.002	0.863 ± 0.001	0.930 ± 0.004	0.871 ± 0.001	0.959 ± 0.002	0.921 ± 0.006
Size(Mb)	27.5	1465	59.9	2138	92.8	3493	111	4275

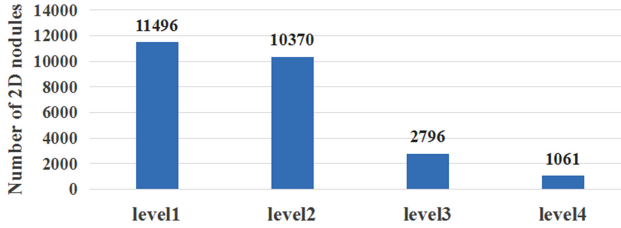


Fig. 12. The distribution of nodules of four different levels in the LIDC/IDRI data set.

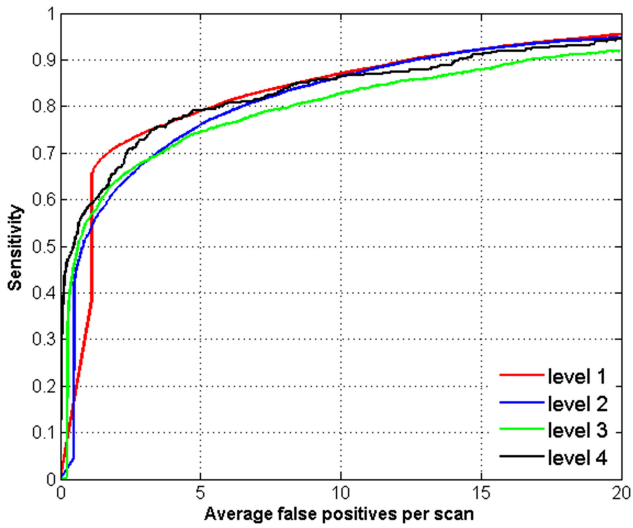


Fig. 13. FROC curves of four levels of nodules classified by this study.

designed by Vedaldi *et al.* [39]. The training parameters including number of epochs, number of batches, momentum and weight decay were set to 10, 50, 0.9, 0.0005 respectively. Besides, the learning rate was set to 0.02, 0.01, 0.005, 0.0025, 0.001 corresponding to the first five epochs and the learning rate in the next epochs was set to 0.001.

To better illustrate the performance of this method, we listed other researches for comparison, which is shown in Table III. This study exploited the whole LIDC/IDRI for the test. After excluding invalid cases (without annotation), we finally obtained 1006 cases that was far more than other researches'. Setio *et al.* [22] and Do *et al.* [43] acquired better results by using multi-view CNN method, but they have excluded the scans whose slice thicknesses are more than 2.5 mm. So, they abandoned the lung nodules that have less 3D information. In addition, they adopted agreement level 3 to define a lung nodule, which means a lung nodule must be accepted by at least 3 radiologists [27].

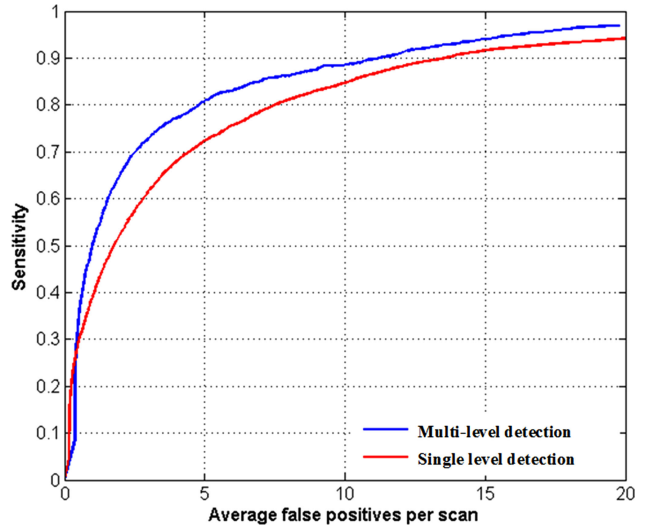


Fig. 14. FROC curves of multi-level detection and single level detection.

TABLE III
PERFORMANCE COMPARISON BETWEEN THIS WORK AND OTHER NODULE DETECTION METHOD

Researches	Sensitivity	FP/scan	Number of Cases
M. Firmino <i>et al.</i> [4]	94.4%	7.04	420
M. Tan <i>et al.</i> [5]	87.5%	4	360
W. J. Choi <i>et al.</i> [6]	97.5%	6.67	84
D. M. Peña <i>et al.</i> [7]	94.23%	0.2	45
D. Cascio <i>et al.</i> [10]	88%	2.5	84
H. Han <i>et al.</i> [17]	89.2%	4.14	205
Teramoto A <i>et al.</i> [19]	90.1%	4.9	84
Setio <i>et al.</i> [22]	85.4% /90.1%	1 /4	888
A. Teramoto <i>et al.</i> [40]	80%	4.2	84
Netto <i>et al.</i> [41]	85.93%	0.138	29
Akbarizadeh G <i>et al.</i> [42]	85.5%	1.99	22
Dou <i>et al.</i> [43]	84.8% /90.7%	1 /4	888
	80.06%	4.7	
This work	/85.06% /90.13% /94%	/6.9 /11.3 /15.1	1006

Hence, some nodules that are not easy to be distinguished were neglected by them to a certain degree. However, this proposed method adopted the standard of agreement level 1 and made full use of 2D information, which had fewer clinical limitations. It is well known that more data will contain more various nodules, which increased the difficulty of detection. Other image

feature descriptors based nodule detection schemes, such as LBP, GLCM, SIFT, Gabor transform, wavelet transform, etc, were suitable for a small range of lung nodules, but lack generalization ability. This study can acquire good detection performance of lung nodules. Through merging the results of four levels of the nodules the average false positives per scan (FP/scan) can be 4.7 with the sensitivity of 80.06%, and the sensitivity can be 94% with the FP/scan of 15.1.

IV. DISCUSSION

The lung nodule detection is the most important step during a course of the lung cancer diagnosis. Facing large amount of data, manual detection took much time and energy. Generally, radiologists had no time to browse each slice carefully, so it was error-prone for them to make diagnosis decisions. However, conventional computer aided nodule detection system need extra processing methods such as nodule segmentation and feature extraction and lacked self-study ability like the human. To excavate and learn the meaningful information from the huge amount of existing data as much as possible, deep learning techniques including deep belief network (DBN) and CNN were introduced into nodule detection and analysis.

CNN was an efficient supervised model for processing a large amount of image data, which can learn the diagnosis knowledge of radiologists. However, some deficiencies were still existed to be solved. First, the input data were unprocessed. Traditional CNN models took multi-scale sub-images that were sampled from raw images as training data. As some disturbing information in images were also learned by CNN models, it was difficult to improve the performance of this model through the long training and the large data set. Especially for medical pathological images, the difference between the nodule region and the non-nodule may be obscure and the interference pixels were random and pervasive. Even though we increased the complexity of the CNN structure, the effect of improvement was quite slight. Second, the accumulation of data can augment the time cost of training. Totally about 20 million sub-images that contained a large amount of unsuspicious sub-images formed the data set Group 1 (see Fig. 9) and part of these unsuspicious sub-images may also affect model's learning efficiency. To automatically detect the accurate position of nodule, it was beneficial to only provide suspicious regions as far as possible, which was the critical task for radiologists.

This study designed two methods to greatly improve the effectiveness of the CNN structure and meanwhile reduce the false positives of nodule detection. First, we applied one kind of vascular enhancement method, i.e. Frangi filter, to eliminate vessel-like structures or other tiny noises. Through observation and comparison, we manually selected appropriate parameters of Frangi filter for displaying the noise-eliminating images without distortion (see Fig. 4). However, the current parameter selection cannot be made automatically based on the special image. It will be helpful if automatic parameter tuning method were developed and added in this study. Second, we processed the original images (Group 1) and created another data set (Group 2) that were binarization processing images cropped from Group 1. Group 2 contained only backgrounds and suspicious regions, which were the same Group1. Through comparing the same

location between Group 1 and Group 2, we can eliminate unsuspicious sub-images (backgrounds) in Group 1. Finally, a total of approximate 0.3 million sub-images were remained in Group 1. Moreover, Group 2 enhanced the outline information of suspicious lung nodules when it was simultaneously fed into the CNN. As was illustrated in the results (see Table II), significant sub-images (Group 1&2) were important for increasing the nodule detection precision. We also classified these nodules into four types: Leve 1 (3 mm to 7 mm), Leve 2 (8 mm to 12 mm), Leve 3 (13 mm to 17 mm) and Leve 4 (greater than 17mm) (see Table I). In fact, the size difference of the nodules was great, thus uniformly treating these nodules without distinction may reduce the learning efficiency. Multi-level learning and detection was a probably good way to solve this problem. Moreover, the comparison experiment validated that the accuracy of multi-level detection can be substantially better than that of single level detection (see Fig. 14).

In this study, we used 2D lung images to design nodules detection method. Although 3D processing can reflect the whole information about the nodules, it will also require more training time and storage space. Besides, sometimes the image 3D reconstruction was required, which was a difficult step. Importantly the CT scans of LIDC/IDRI had different slice thicknesses (0.6 ~ 5 mm), which were not recommended to be uniformly used in 3D nodule detection [44]. On the contrary, 2D lung CT images were not only off-the-peg but also not influenced by the slice thickness. Hence, using 2D image information is a more ideal way to detect the lung nodules.

As a matter of fact, radiologists may also make diagnosis errors such as marking obscure nodule regions, omitting some tiny nodules or mistakenly identifying some nodules. These poor-quality learning materials will influence the learning effect. In this situation, satisfactory performance of the CNN model can be acquired via continually accumulating and updating amounts of exact and crucial diagnosis results.

V. CONCLUSION

This study proposed a novel and efficient computer aided lung nodule automatic detection system, which can extremely reduce false positives. In addition, to avoid missing juxta-pleural nodules, an automatic lung wall mending method was designed by this study. And then another important preprocessing procedure in this work was vascular elimination, which can highlight nodules and meanwhile weaken vessels. To precisely and quickly locate the positions of nodules, four kinds of CNN structures based on four nodule levels were applied. Additionally, two groups of nodule candidates which formed pairs of images (Group 1&2) were the input of the CNN model. Compared with the conventional CNN structure, this method can simplify the data and acquire quite gratifying results by absorbing the merits of two groups of correlative data set (see Table II). Effectively utilizing the abundant diagnosis information that was provided by radiologists and clinician can help us to predict pathological structure of nodules. Since the experiential knowledge of radiologists have been always continually growing and updating, it is greatly important for computer aided systems to keep learning from them. The automatic learning-based nodule detection method of this study will help radiologists to immensely

improve the detection precision when the precious relevance information was uncovered from the big data.

REFERENCES

- [1] L. A. Torre, F. Bray, R. L. Siegel, J. Ferlay, J. Lortet Tieulent, and A. Jemal, "Global cancer statistics, 2012," *CA Cancer J. Clin.*, vol. 65, no. 2, pp. 87–108, 2015.
- [2] I. Sluimer, A. Schilham, M. Prokop, and B. Ginneken, "Computer analysis of computed tomography scans of the lung: A survey," *IEEE Trans. Med. Imag.*, vol. 25, no. 4, pp. 385–405, Apr. 2006.
- [3] H. Y. Jiang, H. Ma, W. Qian, and G. H. Wei, "Risk analysis for pathological changes in pulmonary parenchyma based on lung computed tomography images," *J. Comput. Assist. Tomogr.*, vol. 40, no. 3, pp. 357–363, 2016.
- [4] M. Firmino, G. Angelo, H. Moraes, M. R. Dantas, and R. Valentim, "Computer-aided detection (CADE) and diagnosis (CADx) system for lung cancer with likelihood of malignancy," *Biomed. Eng. Online*, vol. 15, no. 1, 2016, Art. no. 2.
- [5] M. Tan, R. Deklerck, B. Jansen, M. Bister, and J. Cornelis, "A novel computer-aided lung nodule detection system for CT images," *Med. Phys.*, vol. 38, no. 10, pp. 5630–5645, 2011.
- [6] W. J. Choi and T. S. Choi, "Automated pulmonary nodule detection based on three-dimensional shape-based feature descriptor," *Comput. Methods Programs Biomed.*, vol. 113, no. 1, pp. 37–54, 2014.
- [7] D. M. Peña, S. Luo, and A. Abdelgader, "Auto diagnostics of lung nodules using minimal characteristics extraction technique," *Diagnostics*, vol. 6, no. 1, 2016, Art. no. 13.
- [8] E. Taşçı and A. Uğur, "Shape and texture based novel features for automated juxtapleural nodule detection in lung CTs," *J. Med. Syst.*, vol. 39, no. 5, 2015, Art. no. 46.
- [9] A. M. Santos, A. O. de Carvalho Filho, A. C. Silva, A. C. Paiva, R. A. Nunes, and M. Gattass, "Automatic detection of small lung nodules in 3D CT data using Gaussian mixture models, Tsallis entropy and SVM," *Eng. Appl. Artif. Intell.*, vol. 36, pp. 27–39, 2014.
- [10] D. Cascio, R. Magro, F. Fauci, M. Lacomi, and G. Raso, "Automatic detection of lung nodules in CT datasets based on stable 3D mass–spring models," *Comput. Biol. Med.*, vol. 42, no. 11, pp. 1098–1109, 2012.
- [11] S. Sivakumar and C. Chandrasekar, "Lung nodule detection using fuzzy clustering and support vector machines," *Int. J. Eng. Technol.*, vol. 5, no. 1, pp. 179–185, 2013.
- [12] N. Camarlinghi et al., "Combination of computer-aided detection algorithms for automatic lung nodule identification," *Int. J. Comput. Assist. Radiol. Surg.*, vol. 7, no. 3, pp. 455–464, 2012.
- [13] H. C. Shin et al., "Deep convolutional neural networks for computer-aided detection: CNN architectures, dataset characteristics and transfer learning," *IEEE Trans. Med. Imag.*, vol. 35, no. 5, pp. 1285–1298, May 2016.
- [14] R. Anirudh, J. J. Thiagarajan, and T. Bremer, "Lung nodule detection using 3D convolutional neural networks trained on weakly labeled data," *Proc. SPIE Med. Imag.*, vol. 9785, Mar. 2016, Art. no. 978532. [Online]. Available: <http://proceedings.spiedigitallibrary.org/proceeding.aspx?articleid=2507260>
- [15] S. K. Shah et al., "Computer aided characterization of the solitary pulmonary nodule using volumetric and contrast enhancement features 1," *Acad. Radiol.*, vol. 12, no. 10, 1310–1319, 2005.
- [16] F. Ciompi et al., "Bag-of-frequencies: A descriptor of pulmonary nodules in computed tomography images," *IEEE Trans. Med. Imag.*, vol. 34, no. 4, pp. 962–973, Apr. 2015.
- [17] H. Han, L. Li, F. Han, B. Song, W. Moore, and Z. Liang, "Fast and adaptive detection of pulmonary nodules in thoracic CT images using a hierarchical vector quantization scheme," *IEEE J. Biomed. Health Informat.*, vol. 19, no. 2, pp. 648–659, Mar. 2015.
- [18] X. Ye, X. Lin, J. Dehmeshki, G. Slabaugh, and G. Beddoe, "Shape-based computer-aided detection of lung nodules in thoracic CT images," *IEEE Trans. Biomed. Eng.*, vol. 56, no. 7, pp. 1810–1820, Jun. 2009.
- [19] A. Teramoto, H. Fujita, O. Yamamuro, and T. Tamaki, "Automated detection of pulmonary nodules in PET/CT images: Ensemble false-positive reduction using a convolutional neural network technique," *Med. Phys.*, vol. 43, no. 6, pp. 2821–2827, 2016.
- [20] W. Sun, B. Zheng, and W. Qian, "Computer aided lung cancer diagnosis with deep learning algorithms," *Proc. SPIE Med. Imag.*, vol. 9785, Mar. 2016, Art. no. 97850Z. [Online]. Available: <http://proceedings.spiedigitallibrary.org/proceeding.aspx?articleid=2507187>
- [21] T. Jia, H. Zhang, and Y. K. Bai, "Benign and malignant lung nodule classification based on deep learning feature," *J. Med. Imag. Health Informat.*, vol. 5, no. 8, pp. 1936–1940, 2015.
- [22] A. A. A. Setio et al., "Pulmonary nodule detection in ct images: false positive reduction using multi-view convolutional networks," *IEEE Trans. Med. Imag.*, vol. 35, no. 5, pp. 1160–1169, May 2016.
- [23] K. L. Hua, C. H. Hsu, S. C. Hidayati, W. H. Cheng, and Y. J. Chen, "Computer-aided classification of lung nodules on computed tomography images via deep learning technique," *Onco Targets Therapy*, vol. 8, pp. 2015–2022, 2015.
- [24] Y. LeCun, Y. Bengio, and G. Hinton, "Deep learning," *Nature*, vol. 521, no. 7553, pp. 436–444, 2015.
- [25] S. G. Armato III et al., "The lung image database consortium (LIDC) and image database resource initiative (IDRI): A completed reference database of lung nodules on CT scans," *Med. Phys.*, vol. 38, no. 2, pp. 915–931, 2011.
- [26] P. Mildenberger, M. Eichelberg, and E. Martin, "Introduction to the DICOM standard," *Euro. Radiol.*, vol. 12, no. 4, pp. 920–927, 2002.
- [27] R. Golan, C. Jacob, and J. Denzinger, "Lung nodule detection in CT images using deep convolutional neural networks," in *Proc. 2016 Int. Joint Conf. Neural Netw.*, 2016, pp. 243–250.
- [28] C. J. Veenman, M. J. T. Reinders, and E. Backer, "A maximum variance cluster algorithm," *IEEE Trans. Pattern Anal. Mach. Intell.*, vol. 24, no. 9, pp. 1273–1280, Sep. 2002.
- [29] G. Dougherty, "Morphological image processing," in *Digital Image Processing for Medical Applications*, Cambridge, U.K.: Cambridge Univ. Press, 2009, pp. 273–301.
- [30] Y. Sato et al., "Three-dimensional multi-scale line filter for segmentation and visualization of curvilinear structures in medical images," *Med. Image Anal.*, vol. 2, no. 2, pp. 143–168, 1998.
- [31] R. Manniesing, M. A. Viergever, and W. J. Niessen, "Vessel enhancing diffusion: A scale space representation of vessel structures," *Med. Image Anal.*, vol. 10, no. 6, pp. 815–825, 2006.
- [32] A. Frangi, "Three-dimensional model-based analysis of vascular and cardiac images," Ph.D. dissertation, Utrecht Univ., Utrecht, The Netherlands, 2001.
- [33] C. Kirbas and F. Quek, "A review of vessel extraction techniques and algorithms," *ACM Comput. Surv.*, vol. 36, no. 2, pp. 81–121, 2004.
- [34] M. M. Fraz et al., "Blood vessel segmentation methodologies in retinal images—A survey," *Comput. Methods Programs Biomed.*, vol. 108, no. 1, pp. 407–433, 2012.
- [35] M. Sofka and C. V. Stewart, "Retinal vessel centerline extraction using multiscale matched filters, confidence and edge measures," *IEEE Trans. Med. Imag.*, vol. 25, no. 12, pp. 1531–1546, Dec. 2006.
- [36] A. Kerkeni, A. Benabdallah, A. Manzanera, and M. H. Bedoui, "A coronary artery segmentation method based on multiscale analysis and region growing," *Comput. Med. Imag. Graph.*, vol. 48, pp. 49–61, 2016.
- [37] A. Krizhevsky, I. Sutskever, and G. E. Hinton, "Imagenet classification with deep convolutional neural networks," in *Proc. 25th Int. Conf. Neural Inf. Process. Syst.*, 2012, pp. 1097–1105.
- [38] W. Shen et al., "Multi-crop convolutional neural networks for lung nodule malignancy suspiciousness classification," *Pattern Recogn.*, vol. 61, pp. 663–673, 2017.
- [39] A. Vedaldi and K. Lenc, "Matconvnet: Convolutional neural networks for matlab," in *Proc. 23rd ACM Int. Conf. Multimedia*, 2015, pp. 689–692.
- [40] A. Teramoto and H. Fujita, "Fast lung nodule detection in chest CT images using cylindrical nodule-enhancement filter," *Int. J. Comput. Assist. Radiol. Surg.*, vol. 8, no. 2, pp. 193–205, 2013.
- [41] S. M. B. Netto, A. C. Silva, R. A. Nunes, and M. Gattass, "Automatic segmentation of lung nodules with growing neural gas and support vector machine," *Comput. Biol. Med.*, vol. 42, no. 11, pp. 1110–1121, 2012.
- [42] G. kbarizadeh and A. E. Moghaddam, "Detection of lung nodules in CT scans based on unsupervised feature learning and fuzzy inference," *J. Med. Imag. Health Informat.*, vol. 6, no. 2, pp. 477–483, 2016.
- [43] Q. Dou, H. Chen, L. Yu, J. Qin, and P. A. Heng, "Multi-level contextual 3D CNNs for false positive reduction in pulmonary nodule detection," *IEEE Trans. Biomed. Eng.*, vol. 64, no. 7, pp. 1558–1567, Jul. 2017. DOI [10.1109/TBME.2016.2613502](https://doi.org/10.1109/TBME.2016.2613502).
- [44] D. P. Naidich et al., "Recommendations for the management of subsolid pulmonary nodules detected at CT: A statement from the Fleischner society," *Radiology*, vol. 266, pp. 304–317, 2013.